



## Article

# Core Nanoparticle Engineering for Narrower and More Intense Band-Edge Emission from AgInS<sub>2</sub>/GaS<sub>x</sub> Core/Shell Quantum Dots

Watcharaporn Hoisang <sup>1</sup>, Taro Uematsu <sup>1</sup>, Takahisa Yamamoto <sup>2</sup>, Tsukasa Torimoto <sup>3</sup>  
and Susumu Kuwabata <sup>1,\*</sup>

<sup>1</sup> Department of Applied Chemistry, Graduate School of Engineering, Osaka University, 2-1 Yamada-oka, Suita, Osaka 565-0871, Japan; hwatcharaporn@chem.eng.osaka-u.ac.jp (W.H.); t-uematsu@chem.eng.osaka-u.ac.jp (T.U.)

<sup>2</sup> Department of Quantum Engineering, Graduate School of Engineering, Nagoya University, Chikusa-ku, Nagoya 464-8603, Japan; yamamoto.takahisa@material.nagoya-u.ac.jp

<sup>3</sup> Department of Crystalline Materials Science, Graduate School of Engineering, Nagoya University, Chikusa-ku, Nagoya 464-8603, Japan; torimoto@chembio.nagoya-u.ac.jp

\* Correspondence: kuwabata@chem.eng.osaka-u.ac.jp; Tel.: +81-6-6879-7374

Received: 11 November 2019; Accepted: 10 December 2019; Published: 11 December 2019

**Abstract:** Highly luminescent silver indium sulfide (AgInS<sub>2</sub>) nanoparticles were synthesized by dropwise injection of a sulfur precursor solution into a cationic metal precursor solution. The two-step reaction including the formation of silver sulfide (Ag<sub>2</sub>S) nanoparticles as an intermediate and their conversion to AgInS<sub>2</sub> nanoparticles, occurred during the dropwise injection. The crystal structure of the AgInS<sub>2</sub> nanoparticles differed according to the temperature of the metal precursor solution. Specifically, the tetragonal crystal phase was obtained at 140 °C, and the orthorhombic crystal phase was obtained at 180 °C. Furthermore, when the AgInS<sub>2</sub> nanoparticles were coated with a gallium sulfide (GaS<sub>x</sub>) shell, the nanoparticles with both crystal phases emitted a spectrally narrow luminescence, which originated from the band-edge transition of AgInS<sub>2</sub>. Tetragonal AgInS<sub>2</sub> exhibited narrower band-edge emission (full width at half maximum, FWHM = 32.2 nm) and higher photoluminescence (PL) quantum yield (QY) (49.2%) than those of the orthorhombic AgInS<sub>2</sub> nanoparticles (FWHM = 37.8 nm, QY = 33.3%). Additional surface passivation by alkylphosphine resulted in higher PL QY (72.3%) with a narrow spectral shape.

**Keywords:** silver indium sulfide; I–III–VI semiconductor; quantum dots; dropwise injection method; band-edge emission

## 1. Introduction

Luminescent semiconductor nanoparticles, or quantum dots (QDs), have attracted attention over the past two decades due to their unique optical and electronic properties owing to the quantum size effect [1,2]. The optical properties of QDs represented by tunable emission colors on the basis of size and/or composition, high absorption coefficient, and high photoluminescence (PL) quantum yield (QY) are the characteristics of these materials [3]. For instance, chalcogenide binary semiconductor QDs (e.g., CdS, CdSe, and PbS) have been investigated for the use in several optoelectronic and magnetic applications such as wavelength conversion for display devices, light-emitting diodes, chemical sensors, and other spintronic devices [4–8]. However, the high intrinsic toxicity of cadmium (Cd) and lead (Pb) in these QDs limits their potential applications; therefore, alternative materials are needed.

Cadmium-free ternary I–III–VI semiconductor QDs (e.g., AgInS<sub>2</sub> and CuInS<sub>2</sub>) have been intensively investigated to replace cadmium-containing QDs. These cadmium-free QDs possess band

gap energies in the visible region as well as large optical absorption coefficients, which are characteristic for direct semiconductors [9–13]. Among these QDs, silver indium sulfide (AgInS<sub>2</sub>) nanoparticles (NPs) with a band gap energy of 1.87 eV have attracted increasing attention [14,15]. A universal challenge during the synthesis of AgInS<sub>2</sub> NPs is to balance the reactivity of two cationic precursors against one anionic precursor [10,16]. In the past, the thermal decomposition of a single molecular precursor was used to avoid the reactivity problem, which resulted in a high (~50%) PL QY for AgInS<sub>2</sub>-ZnS NPs [17–19]. The limitations of this method are the necessity of designing a molecular precursor for each composition and the difficulty of controlling the particle size and shape due to the complexity of the decomposition process [20]. Alternatively, the reactions of the cation mixture with sulfur-containing species at higher temperatures are common. A typical example uses silver nitrate (AgNO<sub>3</sub>), indium acetate (In(OAc)<sub>3</sub>), and 1-dodecanethiol (DDT) dissolved in 1-octadecene (ODE), which were heated until DDT reacted with metal cations to generate AgInS<sub>2</sub> NPs [21]. Although the “heating up” approach achieved better PL QY, it was still difficult to regulate the particle size because the growth process mainly occurred by Ostwald ripening [22,23]. At the same time, the method of particle size control by the rapid injection of precursors into a hot solvent, which has been commonly used for binary semiconductor QDs, was also adopted for the AgInS<sub>2</sub> NPs synthesis and achieved good size distribution with a PL QY as high as 59% [24–26]. Although the control over particle size and composition was achieved, none of these attempts generated a narrow band-edge emission corresponding to common II–VI semiconductor QDs.

Recently, we have successfully demonstrated a narrow band-edge PL from AgInS<sub>2</sub> NPs by coating them with a gallium sulfide (GaS<sub>x</sub>) shell to passivate the surface of AgInS<sub>2</sub> NPs [27,28]. Although the surface passivation with an amorphous GaS<sub>x</sub> is essential for generating band-edge emission, the PL QY was considerably affected by the properties of the AgInS<sub>2</sub> core NPs. Specifically, the highest QY value of the band-edge emission (56% after the surface passivation with tri-*n*-octylphosphine) was obtained when using the AgInS<sub>2</sub> core particles with a 4-nm diameter and tetragonal phase. These core NPs showed a high PL QY (64%) by themselves, although the spectral shape originated from a broad defect emission. Therefore, we determined that the core and surface of NPs should be defect-free. These preferred AgInS<sub>2</sub> cores were obtained by a two-step reaction using small silver sulfide (Ag<sub>2</sub>S) NPs as intermediate species.

In this study, the dropwise addition of sulfur sources in liquid was adopted instead of adding solid thiourea all at once. This approach was adopted because the control of the reaction speed for both Ag<sub>2</sub>S nucleation and conversion to AgInS<sub>2</sub> is essential to obtain better cores. The speed of injection and reaction temperature were changed to control the particle size and crystal structures of the AgInS<sub>2</sub> cores. The GaS<sub>x</sub> shell coating on the prepared AgInS<sub>2</sub> NPs exhibited band-edge PL, which was still narrower than that in our previous report. The highest PL QY of the as-prepared AgInS<sub>2</sub>/GaS<sub>x</sub> core/shell QDs was ~50%, and the value increased to 70% after the surface treatment with tri-*n*-octylphosphine.

## 2. Materials and Methods

### 2.1. Materials

Silver acetate (Ag(OAc), 99.9%) and 1-dodecanethiol (DDT, 98.0%) were purchased from Fujifilm Wako Pure Chemical, Japan. Indium acetate (In(OAc)<sub>3</sub>, 99.9%) and gallium acetylacetonate (Ga(acac)<sub>3</sub>, 99.9%) were obtained from Sigma-Aldrich, USA. 1,3-dimethylthiourea (DMTU, >97.0%) and tri-*n*-octylphosphine (TOP, >85%) were supplied by Tokyo Chemical Industry, Japan. The above-mentioned chemicals were used as received without further purification. Oleylamine (OAm, >50%) was purchased from Fujifilm Wako Pure Chemical and then purified by vacuum distillation in the presence of calcium hydride.

### 2.2. Instrumental

The temperature of reaction mixtures was measured directly by a thermocouple and was controlled by a heating mantle equipped with a PID controller. UV–Vis absorption and PL spectra

were recorded using a double beam UV–Vis spectrophotometer (JASCO, Japan, V-670) and a fluorospectrometer (JASCO, Japan, FP-8600). Photoluminescence QY was measured by a diode-array spectrometer equipped with an integrating sphere (Hamamatsu, Japan, PMA12). PL lifetimes were recorded with a time-correlated single-photon counting set-up (Hamamatsu, Japan, QuantaTaurus-Tau). The size and morphology of NPs were observed by a transmission electron microscopy (TEM) instrument (Hitachi, Japan, H-7650) at an acceleration voltage of 100 kV. High-resolution TEM (HRTEM) and high-angle annular dark-field scanning transmission electron microscopy (HAADF-STEM) images were taken by a Cs-corrected HR-STEM (JEOL, Japan, JEM-ARM-200F) at an acceleration voltage of 200 kV. Carbon-coated copper TEM grids (Oken-shoji, Japan, HRC-C10) were used for the preparation of TEM samples. X-ray powder diffraction (XRD) patterns were collected by a powder x-ray diffractometer (Rigaku, Japan, SmartLab) equipped with a parallel beam/parallel slit analyzer. The composition of NPs was analyzed by either a scanning electron microscopy (SEM) instrument (Hitachi, Japan, S-3400N) equipped with an energy-dispersive x-ray (EDX) detector (AMETEK, USA, EDAX X1) or an inductively coupled plasma atomic emission spectroscopy (ICP-AES) instrument (Shimadzu, Japan, ICPS-7510).

### 2.3. Synthesis of AgInS<sub>2</sub> Core Nanoparticles by the Immediate Injection Method

Ag(OAc) (0.4 mmol), In(OAc)<sub>3</sub> (0.4 mmol), and DDT (1.2 mmol) were mixed with OAm (8 mL) in a 50 mL two-necked round bottom flask. The mixture was stirred under Ar and heated to 120 °C. 1,3-dimethylthiourea (0.8 mmol) dissolved in OAm (1 mL) was injected into the metal precursors mixture all at once. The temperature of the solution was elevated to 140 °C and kept at this level for 30 min to grow NPs. After the reaction was completed, the solution was cooled to room temperature and centrifuged to remove large particles. For purification, the OAm-capped AgInS<sub>2</sub> NPs were precipitated by the addition of excess methanol and dispersed in chloroform.

### 2.4. Synthesis of AgInS<sub>2</sub> Core NPs by the Dropwise Injection Method

Ag(OAc) (0.4 mmol), In(OAc)<sub>3</sub> (0.4 mmol), and DDT (1.2 mmol) were mixed with OAm (8 mL) in a two-necked round bottom flask. The mixture was heated to 140 °C under Ar, followed by the dropwise injection of 0.4 M DMTU dissolved in OAm using a syringe pump. The flow rate of the injection was varied in the range of 2–16 mL/h, but the total amount was set to 2 mL. The solution temperature was maintained at 140 °C for 30 min after the injection was completed. The solution was then cooled to room temperature, and the purification of the NPs was performed using the above-mentioned approach.

### 2.5. GaS<sub>x</sub> Shell Formation on AgInS<sub>2</sub> Core NPs

AgInS<sub>2</sub>/GaS<sub>x</sub> core/shell NPs were synthesized according the method described in our previous report with slight modifications [27]. Typically, AgInS<sub>2</sub> core NPs (30 nmol in terms of particles), Ga(acac)<sub>3</sub> (0.1 mmol), and DMTU (0.1 mmol) were mixed with OAm (7 mL), and the solution was degassed under vacuum. Under an Ar atmosphere, the solution was rapidly heated to 230 °C, and then the temperature was increased to 280 °C at a rate of 2 °C/min. The color of the solution changed from red to orange, which indicated that the GaS<sub>x</sub> shell was formed on the AgInS<sub>2</sub> core surface. The reaction mixture was allowed to cool to room temperature, and the core/shell NPs were purified by the addition of methanol to precipitate the NPs, followed by centrifugation and dispersion in chloroform. Finally, TOP was added to the core/shell NP solutions 1:1 to chloroform and the mixed solutions were maintained at room temperature to complete post-treatment (caution: TOP can be flammable if a small spill is wiped up with a Kimwipe).

### 3. Results and Discussion

#### 3.1. Synthesis of High-Quality AgInS<sub>2</sub> Quantum Dots

In our previous procedures for synthesizing AgInS<sub>2</sub> cores, thiourea solid was put directly into the metal precursor solution. To better control particle size and composition during the synthesis of ternary NPs, it is essential to control the nucleation of intermediate Ag<sub>2</sub>S NPs. As thiourea is barely soluble in oleylamine and the lowest polarity solvent used for synthesizing NPs, an alternative sulfur source with similar reactivity, 1,3-dimethylthiourea (DMTU), was adopted. The AgInS<sub>2</sub> core QDs were synthesized by introducing the oleylamine solution of DMTU into preheated metal precursor solutions. Two types of injection methods were attempted (i.e., immediate and dropwise injections). The immediate injection method is similar to the hot injection method, which is commonly used for synthesizing II–VI semiconductors. However, as a result of empirical optimization, the temperature at which the DMTU solution was injected, was considerably lower (120 °C) than that typically used for II–VI semiconductors (>200 °C). Another dropwise injection method followed the solid thiourea method that takes advantage of the slow dissolution of solid thiourea to release sulfur. In both cases, when the DMTU solution was injected, a pale-yellow solution (Ag–dodecanethiol complex) became orange, red, and finally dark brown, which indicated the formation of the Ag<sub>2</sub>S intermediate. The Ag<sub>2</sub>S intermediate was subsequently converted to AgInS<sub>2</sub> by cation exchange or resource–host-type reactions [29,30].

Figure 1 shows the UV–Vis, PL spectra, and TEM images and size distribution histograms of AgInS<sub>2</sub> QDs synthesized by the immediate injection and dropwise injection methods. In the immediate injection method, the reaction temperature was increased from 120 °C (injection temperature) to 140 °C to induce the step-by-step growth of Ag<sub>2</sub>S NP and conversion to AgInS<sub>2</sub>. On the other hand, in the dropwise injection method, the temperature of the metal precursor solution remained at 140 °C throughout the reaction, to which DMTU solution (2 mL) was slowly injected at a rate of 4 mL/h. After finishing the injection, the heating was continued for an additional 30 min to complete the conversion from Ag<sub>2</sub>S to AgInS<sub>2</sub>. After centrifugation to remove large insoluble particles, dark-red clear solutions were obtained, regardless of the injection methods. Both types of samples contained nearly monodisperse NPs. The average particle size was slightly smaller (4.6 nm) and PL QY was higher (63.4%) for the NPs synthesized by the dropwise injection method than those synthesized by the immediate injection method (average size = 5.0 nm and PL QY = 50%). The XRD patterns of both samples consisted of three broad peaks at  $2\theta = 26.8^\circ$ ,  $44.8^\circ$ , and  $52.2^\circ$ , which correspond to the (112), (204), and (312) planes of tetragonal AgInS<sub>2</sub>, respectively (Figure 2). However, the large particles removed by centrifugation exhibited small, broad XRD peaks, which are partly attributed to acanthite Ag<sub>2</sub>S and In(OH)<sub>3</sub>; the latter may have originated from indium acetylacetonate. Typically, in colloid synthesis, an immediate injection of reaction species is effective for the separation of nucleation and growth processes to obtain monodisperse NPs. The dropwise injection of precursors was adopted for the synthesis of NP shells to keep the concentration of reactive species low and to prevent nucleation. However, the particle size distribution of AgInS<sub>2</sub> QDs synthesized by the two different methods was similar, and both cases resulted in a size distribution as narrow as  $\sigma = 0.5$  nm. The effectiveness of the dropwise method in terms of size control and higher PL QY may be related to the unique two-step reaction mechanism during which AgInS<sub>2</sub> NPs are formed through an intermediate Ag<sub>2</sub>S. In other words, Ag<sub>2</sub>S NPs or clusters needed to be quickly converted to silver indium sulfide after the formation, otherwise they become too large and precipitate out in the reaction solution.

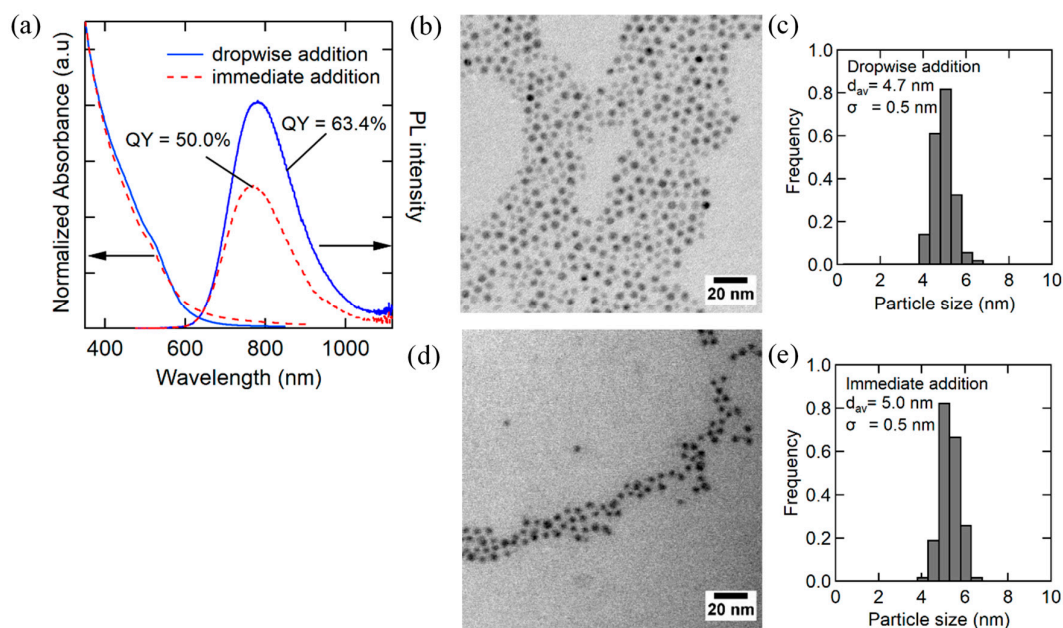


**Figure 1.** (a) UV-Vis absorption and photoluminescence (PL) spectra of AgInS<sub>2</sub> core nanoparticles (NPs) synthesized by different modes for 1,3-dimethylthiourea (DMTU) addition; (red line) immediate injection and (blue line) dropwise injection at 4 mL/h to metal precursor solution heated at 140 °C. Transmission electron microscopy (TEM) images and the corresponding size distribution histograms of AgInS<sub>2</sub> NPs prepared by (b,c) immediate and (d,e) dropwise injection.

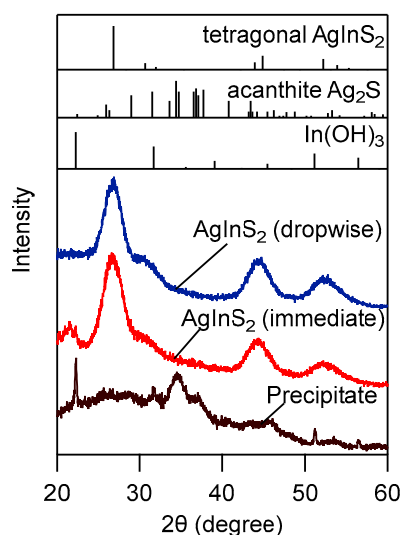


**Figure 2.** X-ray powder diffraction (XRD) patterns of AgInS<sub>2</sub> NPs synthesized by different methods; (red line) immediate and (blue line) dropwise injection methods; 4 mL/h injection rate into a metal precursor solution that was heated to 140 °C; (brown line) large particles, which were separated after the reaction. XRD patterns of tetragonal-AgInS<sub>2</sub> (ICSD 077-6632), acanthite Ag<sub>2</sub>S (ICSD 014-0072), and In(OH)<sub>3</sub> (ICSD 085-1338) are presented as references.

The elemental compositions of AgInS<sub>2</sub> QDs prepared by the immediate and dropwise injection methods were measured using SEM-EDX, and the results are shown in Figure S1 (Supplementary Materials). The atomic ratio of the sample prepared by the immediate injection of the sulfur source

was Ag:In:S = 1:0.69:1.75, whereas Ag:In:S = 1:0.9:2.2 with a more stoichiometric ratio was obtained for the NPs prepared by the dropwise injection method. The conversion from Ag<sub>2</sub>S to AgInS<sub>2</sub> was relatively slower than the formation of Ag<sub>2</sub>S. In addition, intermediate Ag<sub>2</sub>S NPs were easily overgrown at 140 °C, as predicted by the report that Ag<sub>2</sub>S nanoparticles can be produced at room temperature [30]. Therefore, a portion of the Ag<sub>2</sub>S NPs remained in solution with an imperfect conversion to AgInS<sub>2</sub>, which increased the silver content when a large amount of Ag<sub>2</sub>S NPs was produced by the immediate injection method.

### 3.2. Effect of Injection Rate on the Dropwise Injection Method

The effect of the additional speed of DMTU was investigated by varying the injection rate of a syringe pump in the range of 2–16 mL/h. Figure 3 shows the TEM images and XRD patterns of AgInS<sub>2</sub> QDs synthesized using different DMTU injection rates. Size histograms corresponding to each sample are presented in Figure S2. Highly monodispersed spherical NPs ( $d_{av} = 3\text{--}4\text{ nm}$ ,  $\sigma < 0.5\text{ nm}$ ) were observed for the samples prepared using 2, 4, and 8 mL/h flow rates. The sample prepared at 16 mL/h was slightly large and polydisperse ( $4.6 \pm 0.7\text{ nm}$ ), while the injection rate of 4 mL/h produced the smallest monodisperse AgInS<sub>2</sub> NPs ( $d_{av} = 3.2\text{ nm}$ ,  $\sigma = 0.3\text{ nm}$ ). A further decrease in the injection rate (2 mL/h) increased the contribution of the Oswald ripening, which increased polydispersity. The XRD patterns showed a good agreement with those of tetragonal AgInS<sub>2</sub>, except for the samples prepared at 16 mL/h (Figure 3e). Furthermore, elemental analyses of each sample revealed a 1:1 inclusion of Ag:In except for the sample prepared at 16 mL/h (Ag:In = 1:0.2), which suggests that large spherical objects observed in Figure 3d primarily consisted of unconverted Ag<sub>2</sub>S NPs (Table S1).

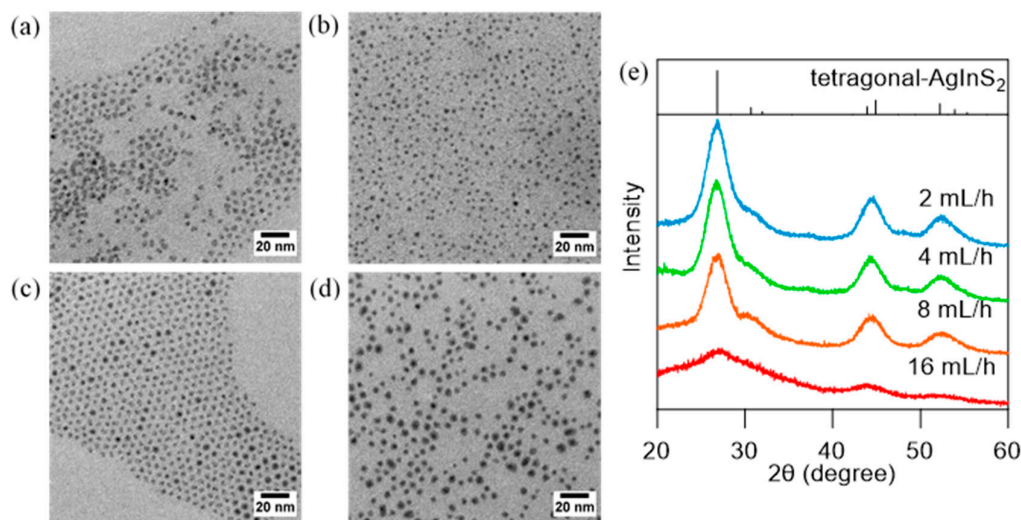


**Figure 3.** TEM images of AgInS<sub>2</sub> NPs prepared by dropwise addition of DMTU at flow rate of (a) 2 mL/h, (b) 4 mL/h, (c) 8 mL/h, and (d) 16 mL/h. (e) XRD patterns of AgInS<sub>2</sub> NPs prepared by dropwise injection method at various flow rate of DMTU addition: (blue) 2 mL/h, (green) 4 mL/h, (orange) 8 mL/h, and (red) 16 mL/h. XRD patterns of tetragonal-AgInS<sub>2</sub> (ICSD 077-6632) is presented as reference.

Figures 4a,b show the UV-Vis and PL spectra of AgInS<sub>2</sub> QDs corresponding to the samples in Figure 3, together with the variation in PL QYs and PL full widths at half maximum (FWHMs) of each sample (Figure 4c). Unlike many previous studies on AgInS<sub>2</sub> NPs, small excitonic absorption shoulders were observed at ~520 nm for the three samples synthesized using an injection rate smaller than 8 mL/h. This feature disappeared for the sample synthesized at 16 mL/h, and the longer absorption tail emerged (Figure 4a). The appearance of the excitonic peak is generally due to the formation of well-defined NPs with a narrow size distribution and minimal defect sites [31], and



these three samples exhibited high PL QYs of over 60%. On the other hand, a distorted broad spectrum with a relatively low PL QY (20%) was obtained for the 16 mL/h sample (Figure 4b), which was mostly comprised of Ag<sub>2</sub>S. These results demonstrate the advantages of the dropwise injection method against the immediate injection method in terms of avoiding the overgrowth of the intermediate Ag<sub>2</sub>S NPs.

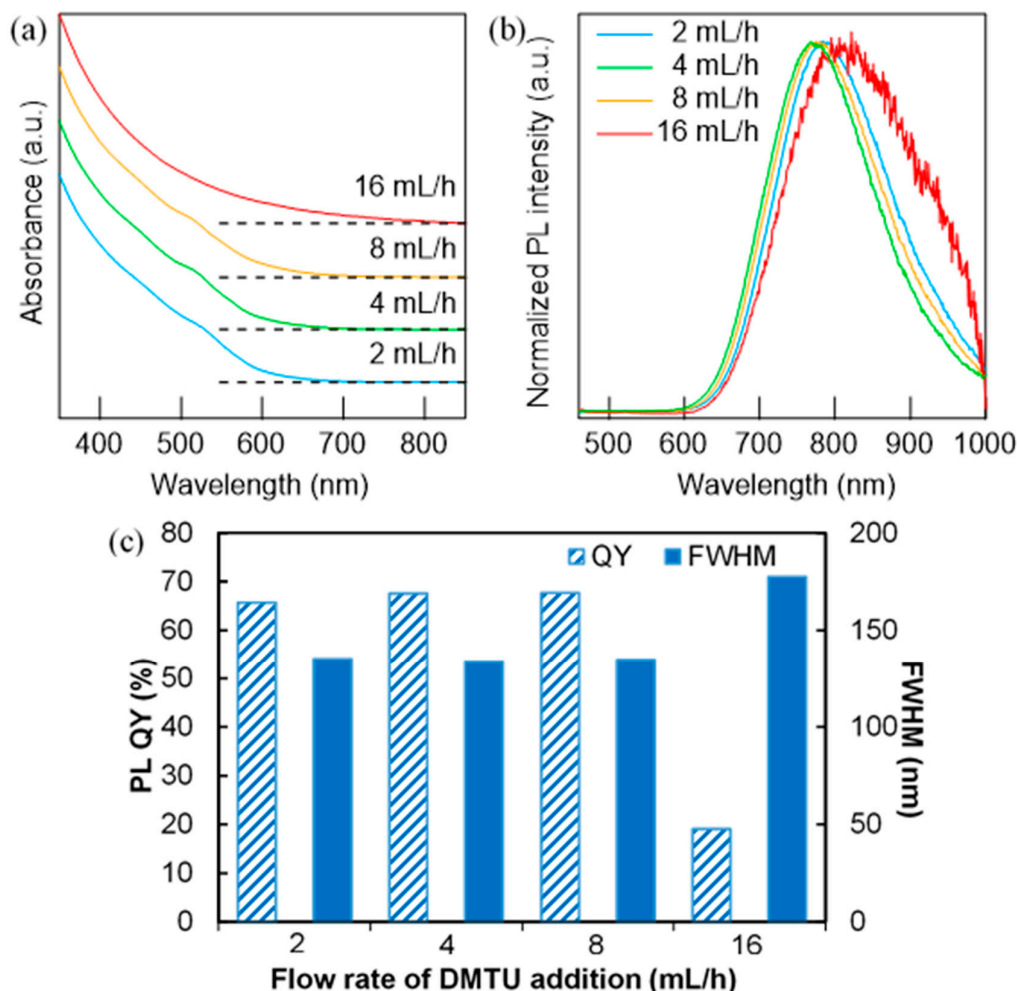


**Figure 4.** (a) UV-Vis absorption and (b) PL spectra of AgInS<sub>2</sub> NPs prepared by the dropwise injection method with a different flow rate of DMTU (2–16 mL/h). (c) Comparison of the PL quantum yield (QY) and full width at half maximum (FWHM) of AgInS<sub>2</sub> NPs prepared at different flow rates of DMTU.

As above-mentioned, the role of the post-heat treatment is to complete the conversion of Ag<sub>2</sub>S to AgInS<sub>2</sub>. Figures 5a,b show the UV-Vis and PL spectra obtained at different durations of post-heat treatment between 0 and 60 min. The edge of the absorption, which was initially located at >850 nm due to the existence of Ag<sub>2</sub>S NPs [32], blue-shifted with an increase in heating time, and excitonic shoulders at approximately 500 nm became distinct. The NPs were non-luminescent at 0 min (just after the injection was finished), but they started to emit and blue-shifted to 780 nm. The PL QY increased rapidly to 66% after 15 min (Figure 5c), and the absorption tail was similar to that of pure AgInS<sub>2</sub>, and it remained with a slight redshift of the PL (Figure 5b). During heating, after the purification by centrifugation, the color density of the solution considerably changed (Figure 5d) and monotonically increased after 15 min while maintaining a constant absorption profile. Using the adopted reaction conditions, the intermediate Ag<sub>2</sub>S NPs exhibited lower solubility than that of the AgInS<sub>2</sub> NPs, which was favorable for obtaining a product without complicated purification processes.

Therefore, the first increase in solution color density indicates the conversion progress to AgInS<sub>2</sub> NPs. At the same time, the increase in particle size and change in the crystal phase occurred. These tendencies became more pronounced after 30 min, as shown in the TEM images and size histograms in Figure S3. The average diameter of the NPs increased by approximately 2 nm, with an increase in size distribution ( $\sigma \sim 0.8$  nm), which indicates the occurrence of the Ostwald ripening. The XRD pattern shows a change in the crystal phase from tetragonal to orthorhombic during the last 30 min.

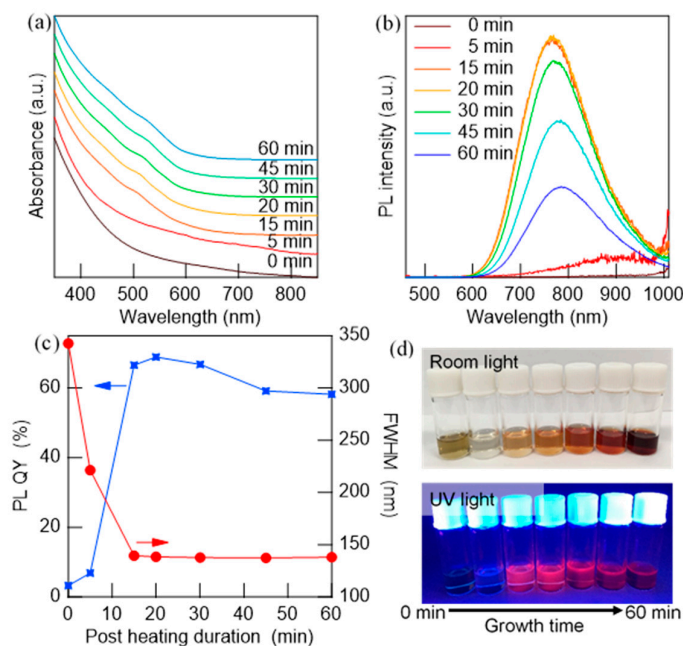


**Figure 5.** Evolution of (a) UV–Vis and (b) PL spectra of AgInS<sub>2</sub> NPs at 140 °C with time after completing the dropwise injection of DMTU (4 mL/h, 0–60 min). (c) Change in PL QY values and PL FWHM as a function of growth time (post-heating), and the (d) corresponding photographs under room light (**upper**) and UV light (**bottom**).

### 3.3. Effect of Temperature on the Generation of AgInS<sub>2</sub> QDs by DMTU Injection

The effects of reaction temperature were investigated in relation to the luminescence performance and morphology of AgInS<sub>2</sub> QDs. The synthesis was carried out by adding DMTU (flow rate, 4 mL/h) into the metal precursor solution heated at 130–180 °C. In all experiments, the solution temperature was maintained for an additional 30 min after the dropwise injection was completed. Figure 6a shows the PL spectra of the AgInS<sub>2</sub> QDs synthesized at different reaction temperatures along with the PL QY of each sample. The QDs synthesized at 130 °C did not exhibit PL, which is consistent with the absence of AgInS<sub>2</sub> features in XRD (Figure 6b). The highest PL QY was obtained at 140 °C, above which the PL QY gradually decreased (Figure 6a and Table 1). In this temperature region, an increase in the particle size and the transformation of the crystal phase from tetragonal to orthorhombic were observed (Figures 6b and 7).



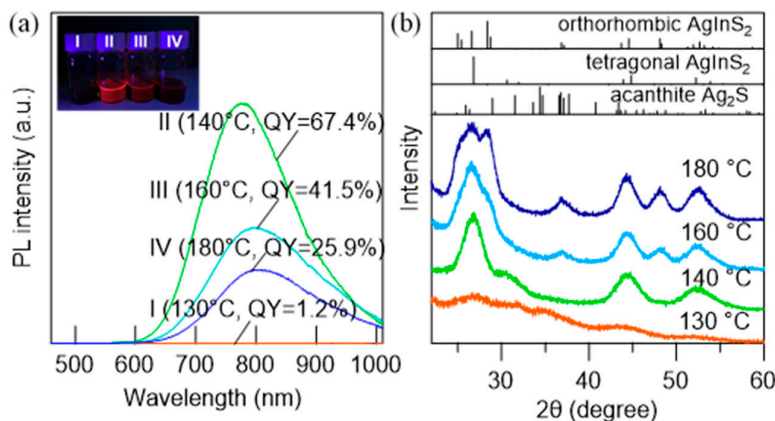


**Figure 6.** (a) PL spectra of AgInS<sub>2</sub> NPs prepared at different reaction temperatures ranging from 130 to 180 °C using the dropwise injection method (4 mL/h). The PL QYs for each sample are displayed in the same figure. The inset shows photographic images of the corresponding AgInS<sub>2</sub> NP solutions under UV light. (b) XRD patterns of the AgInS<sub>2</sub> NP samples at different reaction temperatures (130–180 °C), which correspond to the reference patterns of tetragonal-AgInS<sub>2</sub> (ICSD 077-6632), orthorhombic-AgInS<sub>2</sub> (ICSD 070-5630), and acanthite Ag<sub>2</sub>S (ICSD 014-0072).

**Table 1.** Atomic ratios of the elements and the properties of the AgInS<sub>2</sub> NPs prepared at different temperatures of 130–180 °C.

Reaction Temperature (°C)	Measured Atomic Ratios			PL QY (%)	FWHM (nm)
	Ag	In	S		
130	1	0.74	2.40	1.2	259.4
140	1	1.11	2.46	67.4	137.1
160	1	1.05	2.30	41.5	143.5
180	1	0.98	2.11	25.9	142.9

As reported previously, annealing at higher temperatures caused the disordering of cations, which induced the transformation into the orthorhombic phase [19,30]. Figure S4 shows the UV–Vis spectra and the corresponding Tauc plots. The three samples (prepared at 140–180 °C) produced the Tauc plots for a direct semiconductor, which included well-defined straight regions from which the band gap values ( $E_g$ ) were estimated to be 2.11–2.14 eV. However, the NPs synthesized at 130 °C exhibited an absorption tail at >850 nm, which corresponded to the remaining intermediate Ag<sub>2</sub>S with a band gap of 1.1 eV [33]. The elemental composition of NPs supported similar assumptions (Table 1) that are discussed above, indicating that the less reactive indium species needs a temperature higher than 140 °C to be fully incorporated in nanoparticles. Specifically, the condition of 140 °C with 30 min for post-heating was optimal for synthesizing small tetragonal AgInS<sub>2</sub> NPs because (i) the formation of Ag<sub>2</sub>S intermediate NPs was sufficiently slow to maintain their small size, and (ii) the conversion from Ag<sub>2</sub>S to AgInS<sub>2</sub> NPs using indium sulfide clusters was barely possible. The conversion using these cluster species has been reported as a resource–host-type reaction [34]. At higher temperatures, the excessive growth of the intermediate Ag<sub>2</sub>S NPs resulted in an increase in the size of AgInS<sub>2</sub> NPs, or the Ostwald ripening of the AgInS<sub>2</sub> NPs generated using this approach may produce unfavorable results [35,36].

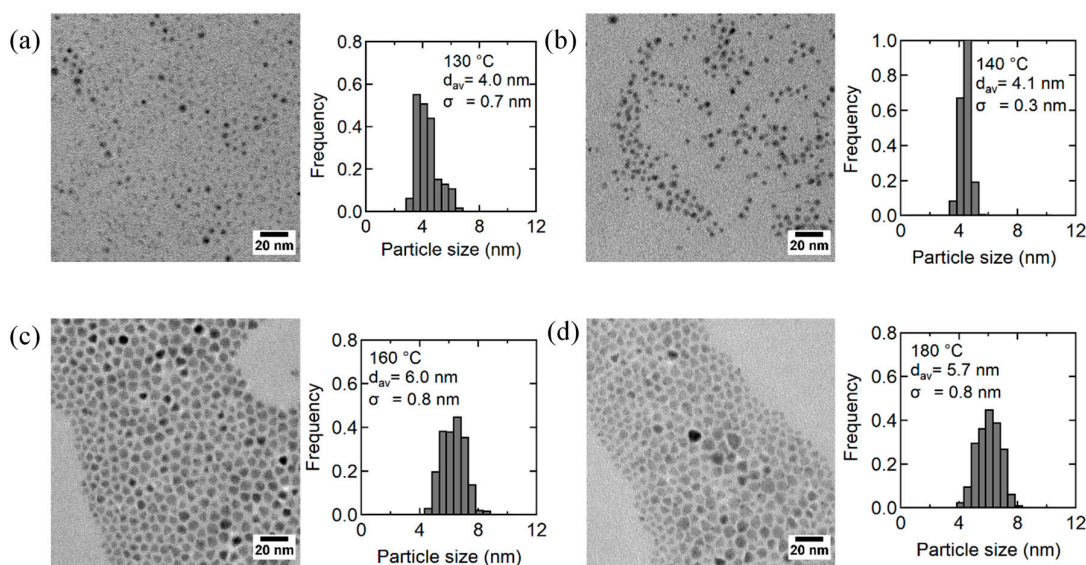


**Figure 7.** TEM images and the corresponding size distribution histograms for AgInS<sub>2</sub> NPs prepared by the dropwise injection method (4 mL/h) at different reaction temperatures: (a) 130 °C, (b) 140 °C, (c) 160 °C, and (d) 180 °C.

### 3.4. Band-Edge Emission by Surface Passivation with Gallium Sulfides

The tetragonal and orthorhombic AgInS<sub>2</sub> QDs synthesized by the dropwise injection method at different temperatures were coated with gallium sulfide (GaS<sub>x</sub>) shells. The shell formation was achieved using the above-mentioned approach including heating the AgInS<sub>2</sub> core QDs with the precursors of GaS<sub>x</sub>. Figure 8a shows the UV–Vis spectra for the AgInS<sub>2</sub> cores and AgInS<sub>2</sub>/GaS<sub>x</sub> core/shell QDs with different core crystal phases, which are the two types of cores synthesized at 140 °C and 180 °C. The small absorption tail for the tetragonal AgInS<sub>2</sub> core QDs almost disappeared after they were coated with GaS<sub>x</sub>. Moreover, they showed a slight augmentation of shoulder peaks, which is characteristic of high-quality QDs. On the other hand, the absorption tail for the orthorhombic AgInS<sub>2</sub> NPs was smaller than that for the tetragonal NPs, and the changes in the absorption after the shell formation were limited. The values of the band gap energies determined from the Tauc plots were 2.17 eV for the tetragonal AgInS<sub>2</sub>/GaS<sub>x</sub> and 2.14 eV for orthorhombic AgInS<sub>2</sub>/GaS<sub>x</sub> NPs; these values are the same as those of the original core NPs (Figure S5). The PL spectra for both tetragonal and orthorhombic NPs considerably narrowed after the coating with a GaS<sub>x</sub> shell, and the PL peak energies (582 nm, 2.13 eV for tetragonal and 578 nm, 2.14 eV for orthorhombic) were consistent with the band gap energies estimated from the Tauc plots. Therefore, these peaks were identical to the band-edge PL (Figure 8b) [27]. The intensity and color purity were different for the two crystal phases. Specifically, the tetragonal-AgInS<sub>2</sub>/GaS<sub>x</sub> core/shell QDs showed a higher (PL QY = 49.2%) and narrower (FWHM = 32.2 nm) band-edge emission than those of the orthorhombic core/shell QDs (PL QY = 33.3%, FWHM = 37.8 nm). The tetragonal cores clearly produced a more intense band-edge emission than that of the orthorhombic cores. In addition, the values for the tetragonal-AgInS<sub>2</sub>/GaS<sub>x</sub> core/shell QDs were better than those previously obtained for the same type of the core/shell QDs synthesized using solid thiourea (PL QY = 28.8% and FWHM = 39 nm, without surface treatment by phosphine) [27]. The average values and standard deviations for PL QYs obtained by repeated experiments using three different core synthesis methods are summarized in Figure S6, where the standard deviations ( $\pm\sigma$ ) are represented as error bars. The dropwise method done by the appropriate condition demonstrated the highest QY values both for core QDs and core/shell QDs. The narrower size distribution and well-defined surface structure achieved by the controlled solution-phase

reactions resulted in the increase in the PL QYs and narrowing of the PL FWHM. In addition, the PL enhancement by the post-treatment with tri-*n*-octylphosphine remained valid for these samples. The record-high PL QYs of 72.3% and 51.8% were achieved for the tetragonal and orthorhombic samples, respectively, without any noticeable changes in the UV–Vis profiles (Figure S7). Therefore, this enhancement was attributed to the removal of the trap states, which may be present on the surface of the GaS<sub>x</sub> shells, as we have previously reported [27].

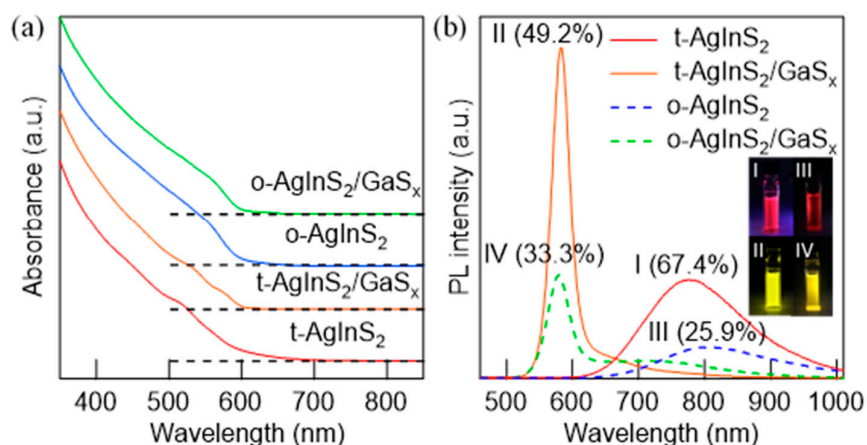


**Figure 8.** (a) UV–Vis absorption and (b) PL spectra with displayed PL QYs for the AgInS<sub>2</sub> cores and AgInS<sub>2</sub>/GaS<sub>x</sub> core/shell NPs produced at various conditions: (I) tetragonal-AgInS<sub>2</sub> core (DMTU flow rate = 4 mL/h at 140 °C and post-heating for 30 min), (II) tetragonal-AgInS<sub>2</sub>/GaS<sub>x</sub> core/shell (prepared from the tetragonal-AgInS<sub>2</sub> core NPs), (III) orthorhombic-AgInS<sub>2</sub> core (DMTU flow rate = 4 mL/h at 180 °C and post-heating for 30 min), and (IV) orthorhombic-AgInS<sub>2</sub>/GaS<sub>x</sub> core/shell (prepared from the orthorhombic-AgInS<sub>2</sub> core NPs). The inset shows the photographs of the AgInS<sub>2</sub> core and AgInS<sub>2</sub>/GaS<sub>x</sub> core/shell NPs in chloroform.

The TEM observations revealed the morphological changes for the AgInS<sub>2</sub>/GaS<sub>x</sub> core/shell QDs of two crystal structures (Figure 9) compared with those of the original cores (Figure S8). The EDX spectrum of the same type of nanoparticles for the area, as shown in Figure S9a, clearly indicated the existence of gallium although the sulfur content was slightly less than the expected values due to the partial oxidation and/or photocorrosion of the sample during repetitive purification processes to remove excess ligand that is inevitable to obtain clear TEM images (Figure S9b). The average size of the tetragonal cores increased by 2.0 nm while maintaining a relatively narrow size distribution ( $\sigma = 0.6$ ). The orthorhombic cores, which possess a more angular shape and wider size distribution than those of the tetragonal cores, also increased their size by 1.6 nm with  $\sigma = 0.9$  nm. The HRTEM and HAADF-STEM images of the corresponding core/shell QDs showed clear lattice fringes and well-organized atomic columns, respectively, for the crystalline core portions (Figures 9b,c,e, and f). The irregular white dots around the cores in the HAADF-STEM images demonstrated the existence of amorphous shells surrounding the crystalline cores (Figures 9c–f). These results are consistent with the XRD patterns of AgInS<sub>2</sub>/GaS<sub>x</sub> core/shell NPs, which were almost unchanged after the formation of GaS<sub>x</sub> shells as shown in Figure S10, indicating the amorphous nature of the shell materials. More accurate composition analyses were performed by using ICP-AES for the purified nanoparticle powders, both before and after coating with GaS<sub>x</sub>, and the results are summarized in Table S2. The Ga:S ratios of 1:0.73 and 1:0.60 for the tetragonal and orthorhombic AgInS<sub>2</sub> cores, respectively, were obtained under the assumption that the core is stoichiometric, where the ratio of sulfur was similar or slightly smaller than that in our previous report owing to the oxidation of the shell surface. The thicker GaS<sub>x</sub> shell (1.0 nm) than that in our previous report (0.6 nm) contributed to the increase in the band-edge emission intensity of the tetragonal AgInS<sub>2</sub> QDs. However, the detailed mechanism of

why GaS<sub>x</sub> shells stick more to the AgInS<sub>2</sub> QDs prepared with the dropwise injection method needs to be revealed.

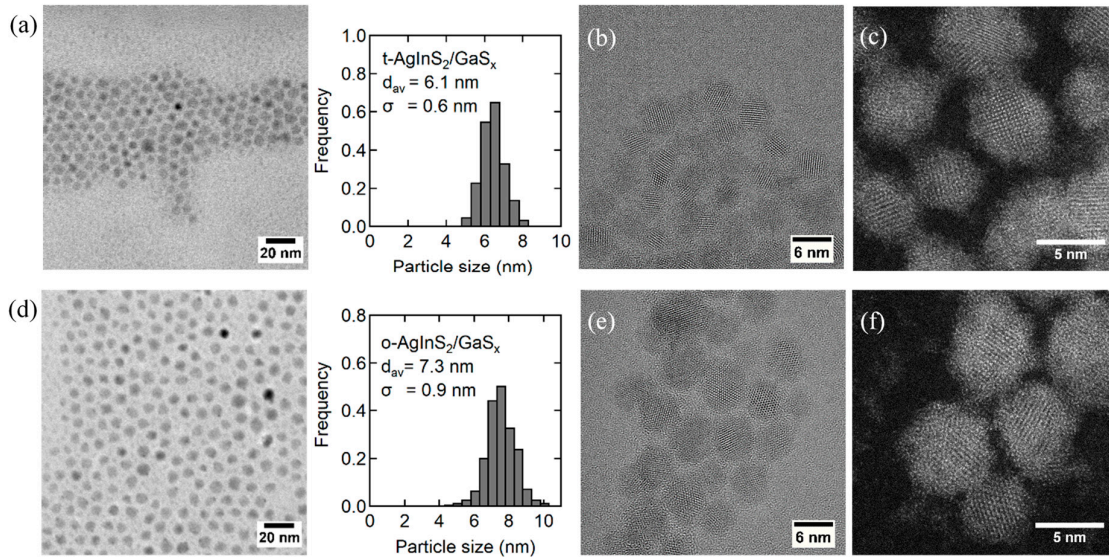


**Figure 9.** (a,d) TEM images and the corresponding size distribution histograms, (b,e) High-resolution TEM (HRTEM) and (c,f) high-angle annular dark-field scanning transmission electron microscopy (HAADF-STEM) images for AgInS<sub>2</sub>/GaS<sub>x</sub> core/shell NPs with different crystal structures; (a–c) tetragonal and (d–f) orthorhombic.

Figure 10 shows the PL decay curves of the AgInS<sub>2</sub> core and AgInS<sub>2</sub>/GaS<sub>x</sub> core/shell NPs with two crystal phases for the core NPs. The PL decay curves for the AgInS<sub>2</sub> core NPs were fitted using either single or biexponential equations.

$$I(t) = \sum_n A_n \exp(-t/\tau_n) \quad (1)$$

where  $I(t)$  is the intensity at time  $t$  and  $A_n$  and  $\tau_n$  represent the amplitude and decay of each component corresponding to  $n$ , respectively. The tetragonal AgInS<sub>2</sub> core NPs can be fit well to a single exponential term with a lifetime of 876 ns (Table 2), which is assignable to the emission from the surface trap-state. The coating of the tetragonal AgInS<sub>2</sub> NPs with GaS<sub>x</sub> resulted in a considerable decrease in lifetimes composed of two equally contributing lifetime components of 37.2 ns and 159 ns (as judged by  $A_n \times \tau_n$ ) when the decay curve was measured at the wavelength of the newly generated narrow peak. The number of lifetime components required to produce a sufficient curve fitting was smaller than that previously reported [27], which suggests that the NP ensemble of higher uniformity was obtained using the dropwise injection method. In comparison to the tetragonal core NPs, the orthorhombic core NPs had two lifetime components (278 ns and 1976 ns), and 95% of the photons originated from the longer lifetime component. However, when the orthorhombic core NPs were passivated by GaS<sub>x</sub>, the decay components became almost identical to the tetragonal-AgInS<sub>2</sub>/GaS<sub>x</sub> core/shell NPs, although the crystal structure of the core remained orthorhombic after it was coated with GaS<sub>x</sub> (Figure S10). We have previously speculated that the longer lifetime component, which is observed for the orthorhombic cores derived from the internal (crystalline) defect levels that cannot be removed by the surface passivation with GaS<sub>x</sub>, and these defect levels decreased the intensity of the band-edge photoluminescence. However, the similarity between the lifetime components of the two crystal phases of the cores after they were coated with the shell evoked a different mechanism. Specifically, the surface of the tetragonal NPs is prone to passivation with GaS<sub>x</sub> when compared with that of the orthorhombic NPs. Further understanding of the



nanostructure interface will help us improve the PL properties of these cadmium-free, ternary semiconductor QDs. This will allow us to produce a replacement for the cadmium-based QDs.

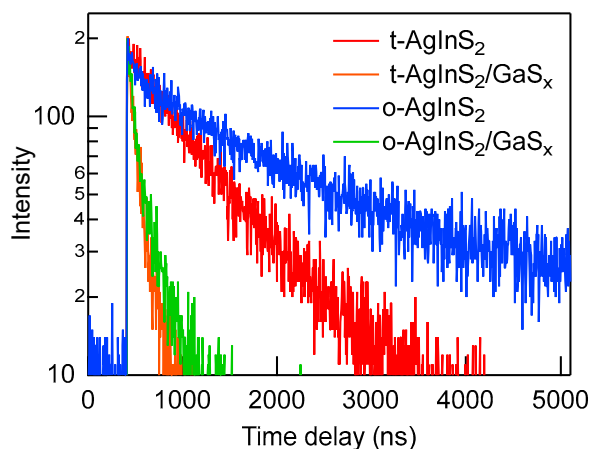


**Figure 10.** PL decay curves of the AgInS<sub>2</sub> core and AgInS<sub>2</sub>/GaS<sub>x</sub> core/shell NPs with two crystal phases for the cores: (red line) tetragonal AgInS<sub>2</sub> core, (orange line) tetragonal-AgInS<sub>2</sub>/GaS<sub>x</sub> core/shell (prepared from the tetragonal-AgInS<sub>2</sub> core), (blue line) orthorhombic-AgInS<sub>2</sub> core, and (green) orthorhombic-AgInS<sub>2</sub>/GaS<sub>x</sub> core/shell (prepared from the orthorhombic-AgInS<sub>2</sub> core). All curves were obtained at the PL peak wavelength of each sample with the excitation at 405 nm.

**Table 2.** PL lifetime components of the AgInS<sub>2</sub> core and AgInS<sub>2</sub>/GaS<sub>x</sub> core/shell NPs corresponding to Figure 10.

NPs <sup>a</sup>	$\lambda_{PL}/nm$	$\tau_1/ns$	$A_1$	$\tau_2/ns$	$A_2$	$\chi^2$
t-AgInS <sub>2</sub>	780	876	1	—	—	1.08
t-AgInS <sub>2</sub> /GaS <sub>x</sub>	582	37.2	0.777	159	0.23	0.98
o-AgInS <sub>2</sub>	803	278	0.29	1976	0.71	1.06
o-AgInS <sub>2</sub> /GaS <sub>x</sub>	578	33.4	0.69	161	0.31	1.00

<sup>a</sup> t-: tetragonal, o-: orthorhombic.

#### 4. Conclusions

We have improved the quality of AgInS<sub>2</sub> core QDs and have successfully enhanced the PL properties of AgInS<sub>2</sub>/GaS<sub>x</sub> core/shell QDs. By injecting the oleylamine solution of thiourea derivative to the solution containing metal-ions, AgInS<sub>2</sub> core NPs were synthesized with high monodispersity. As a result of the studies on reaction mechanism, we have demonstrated that the AgInS<sub>2</sub> NPs were produced through the Ag<sub>2</sub>S intermediate NPs, and the morphology of the AgInS<sub>2</sub> NPs strongly depended on the generation speed of the Ag<sub>2</sub>S NPs and their conversion to AgInS<sub>2</sub>. After the optimization to obtain small AgInS<sub>2</sub> core QDs, highly monodisperse ( $\sigma = 0.3$  nm) AgInS<sub>2</sub> QDs possessing PL QY of 65% was achieved with high reproducibility. In addition, crystal phases of the AgInS<sub>2</sub> QDs could perfectly be controlled by changing reaction temperatures. The passivation of the AgInS<sub>2</sub> QDs with GaS<sub>x</sub> generated a band-edge emission for both tetragonal and orthorhombic core QDs, with the former crystal phase giving a higher PL QY. Eventually, the tetragonal AgInS<sub>2</sub>/GaS<sub>x</sub> core/shell QDs emitted band-edge emission of PL QY as high as 72.3% with a narrow FWHM (32 nm) after the passivation of the GaS<sub>x</sub> shell surface by tri-*n*-octylphosphine. These values are almost equivalent to commercial cadmium-based core/shell QDs, and we expect that the AgInS<sub>2</sub>/GaS<sub>x</sub> core/shell QDs will replace them in the near future.

**Supplementary Materials:** The following are available online at [www.mdpi.com/xxx/s1](http://www.mdpi.com/xxx/s1), Figure S1: EDX spectra of AgInS<sub>2</sub> QDs; Figure S2: Size distribution histograms of AgInS<sub>2</sub> prepared at various injection rates; Figure S3: TEM images and the corresponding size distribution histograms of the AgInS<sub>2</sub> QDs prepared with different annealing time and their XRD patterns; Figure S4: UV–Vis absorption of AgInS<sub>2</sub> NPs prepared at different

reaction temperatures and the corresponding Tauc plots with calculated  $E_g$ ; Figure S5: Tauc plots with calculated  $E_g$  for AgInS<sub>2</sub> cores and AgInS<sub>2</sub>/GaS<sub>x</sub> core/shell NPs with different crystal phases of the cores; Figure S6: Average PL QYs of core and core/shell QDs with standard deviation obtained by repeated experiments; Figure S7: UV–Vis and PL spectra of AgInS<sub>2</sub>/GaS<sub>x</sub> core/shell NPs before and after TOP treatment; Figure S8: TEM images and the corresponding size distribution histograms, HRTEM and HAADF-STEM images for AgInS<sub>2</sub> core NPs; Figure S9: TEM-EDX spectra of tetragonal AgInS<sub>2</sub>/GaS<sub>x</sub> core/shell QDs; and Figure S10: XRD patterns of AgInS<sub>2</sub> core and AgInS<sub>2</sub>/GaS<sub>x</sub> core/shell NPs. Table S1: Atomic ratios of elements and average diameters of AgInS<sub>2</sub> QDs; Table S2: Atomic ratios of elements and average diameters for AgInS<sub>2</sub> cores and AgInS<sub>2</sub>/GaS<sub>x</sub> core/shell NPs.

**Author Contributions:** Writing—original draft preparation, W.H.; Writing—review and editing, T.U.; Analysis—HTEM and STEM, T.Y.; Co-supervision, T.T.; and Supervision, S.K.

**Funding:** This research was supported by the Grant-in-Aid for Scientific Research (A) Grant Number JP18H03863 and Grant-in-Aid for Scientific Research (C) Grant Number JP19K05196.

**Acknowledgments:** This work was supported by the Nichia Corporation. Part of this work (HRTEM and STEM observations) was done by the aid of the MEXT “Nanotechnology Platform” (project no. 12024046).

**Conflicts of Interest:** Two of the research groups represented by S.K. (Osaka University) and T.T. (Nagoya University) have been funded by the Nichia Corporation. The other authors declare that they have no conflicts of interest.

## References

- Murray, C.B.; Norris, D.J.; Bawendi, M.G. Synthesis and characterization of nearly monodisperse CdE (E = sulfur, selenium, tellurium) semiconductor nanocrystallites. *J. Am. Chem. Soc.* **1993**, *115*, 8706–8715, doi:10.1021/ja00072a025.
- Smith, A.M.; Nie, S. Semiconductor nanocrystals: Structure, properties, and band gap engineering. *Acc. Chem. Res.* **2010**, *43*, 190–200, doi:10.1021/ar9001069.
- Zlateva, G.; Zhelev, Z.; Bakalova, R.; Kanno, I. Precise size control and synchronized synthesis of zhelev six colors of CdSe quantum dots in a slow-increasing temperature gradient. *Inorg. Chem.* **2007**, *46*, 6212–6214, doi:10.1021/ic062045s.
- Talapin, D.V.; Lee, J.-S.; Kovalenko, M.V.; Shevchenko, E.V. Prospects of colloidal nanocrystals for electronic and optoelectronic applications. *Chem. Rev.* **2010**, *110*, 389–458, doi:10.1021/cr900137k.
- Medintz, I.L.; Stewart, M.H.; Trammell, S.A.; Susumu, K.; Delehanty, J.B.; Mei, B.C.; Melinger, J.S.; Blanco-Canosa, J.B.; Dawson, P.E.; Mattoussi, H. Quantum-dot/dopamine bioconjugates function as redox coupled assemblies for in vitro and intracellular pH sensing. *Nat. Mater.* **2010**, *9*, 676–684, doi:10.1038/nmat2811.
- Nozik, A.J.; Beard, M.C.; Luther, J.M.; Law, M.; Ellingson, R.J.; Johnson, J.C. Semiconductor quantum dots and quantum dot arrays and applications of multiple exciton generation to third-generation photovoltaic solar cells. *Chem. Rev.* **2010**, *110*, 6873–6890, doi:10.1021/cr900289f.
- Neves, M.C.; Martins, M.A.; Soares-Santos, P.C.R.; Rauwel, P.; Ferreira, R.A.S.; Monteiro, T.; Carlos, L.D.; Trindade, T. Photoluminescent, transparent and flexible di-ureasil hybrids containing CdSe/ZnS quantum dots. *Nanotechnology* **2008**, *19*, 155601, doi:10.1088/0957-4484/19/15/155601.
- Pereira, A.S.; Rauwel, P.; Reis, M.S.; Oliveira Silva, N.J.; Barros-Timmons, A.; Trindade, T. Polymer encapsulation effects on the magnetism of EuS nanocrystals. *J. Mater. Chem.* **2008**, *18*, 4572–4578, doi:10.1039/B806499G.
- Kim, J.-H.; Kim, B.-Y.; Jang, E.-P.; Yoon, S.-Y.; Kim, K.-H.; Do, Y.R.; Yang, H. Synthesis of widely emission-tunable Ag–Ga–S and its quaternary derivative quantum dots. *Chem. Eng. J.* **2018**, *347*, 791–797, doi:10.1016/j.cej.2018.04.167.
- Xie, R.; Rutherford, M.; Peng, X. Formation of high-quality I–III–VI Semiconductor nanocrystals by tuning relative reactivity of cationic precursors. *J. Am. Chem. Soc.* **2009**, *131*, 5691–5697, doi:10.1021/ja9005767.
- Yarema, O.; Yarema, M.; Wood, V. Tuning the composition of multicomponent semiconductor nanocrystals: The case of I–III–VI materials. *Chem. Mater.* **2018**, *30*, 1446–1461, doi:10.1021/acs.chemmater.7b04710.
- Allen, P.M.; Bawendi, M.G. Ternary I–III–VI quantum dots luminescent in the red to near-infrared. *J. Am. Chem. Soc.* **2008**, *130*, 9240–9241, doi:10.1021/ja8036349.
- Li, L.; Daou, T.J.; Texier, I.; Kim Chi, T.T.; Liem, N.Q.; Reiss, P. Highly luminescent CuInS<sub>2</sub>/ZnS core/shell nanocrystals: Cadmium-free quantum dots for in vivo imaging. *Chem. Mater.* **2009**, *21*, 2422–2429, doi:10.1021/cm900103b.



13. Yang, W.; Gong, X.; Chang, J. Development of novel cadmium-free AgInS<sub>2</sub> semiconductor nanoparticles. *J. Nanosci. Nanotechnol.* **2016**, *16*, 2172–2183, doi:10.1166/jnn.2016.10946.
14. Torimoto, T.; Adachi, T.; Okazaki, K.-I.; Sakuraoaka, M.; Shibayama, T.; Ohtani, B.; Kudo, A.; Kuwabata, S. Facile synthesis of ZnS–AgInS<sub>2</sub> solid solution nanoparticles for a color-adjustable luminophore. *J. Am. Chem. Soc.* **2007**, *129*, 12388–12389, doi:10.1021/ja0750470.
15. Regulacio, M.D.; Win, K.Y.; Lo, S.L.; Zhang, S.-Y.; Zhang, X.; Wang, S.; Han, M.-Y.; Zheng, Y. Aqueous synthesis of highly luminescent AgInS<sub>2</sub>–ZnS quantum dots and their biological applications. *Nanoscale* **2013**, *5*, 2322–2327, doi:10.1039/C3NR34159C.
16. Uematsu, T.; Doi, T.; Torimoto, T.; Kuwabata, S. Preparation of luminescent AgInS<sub>2</sub>–AgGaS<sub>2</sub> solid solution nanoparticles and their optical properties. *J. Phys. Chem. Lett.* **2010**, *1*, 3283–3287, doi:10.1021/jz101295w.
17. Torimoto, T.; Ogawa, S.; Adachi, T.; Kameyama, T.; Okazaki, K.-I.; Shibayama, T.; Kudo, A.; Kuwabata, S. Remarkable photoluminescence enhancement of ZnS–AgInS<sub>2</sub> solid solution nanoparticles by post-synthesis treatment. *Chem. Commun.* **2010**, *46*, 2082–2084, doi:10.1039/B924186H.
18. Feng, Z.; Dai, P.; Ma, X.; Zhan, J.; Lin, Z. Monodispersed cation-disordered cubic AgInS<sub>2</sub> nanocrystals with enhanced fluorescence. *Appl. Phys. Lett.* **2010**, *96*, 013104, doi:10.1063/1.3280372.
19. Castro, S.L.; Bailey, S.G.; Raffaele, R.P.; Banger, K.K.; Hepp, A.F. Synthesis and characterization of colloidal CuInS<sub>2</sub> nanoparticles from a molecular single-source precursor. *J. Phys. Chem. B* **2004**, *108*, 12429–12435, doi:10.1021/jp049107p.
20. Chen, S.; Ahmadiantehrani, M.; Zhao, J.; Zhu, S.; Mamalis, A.G.; Zhu, X. Heat-up synthesis of Ag–In–S and Ag–In–S/ZnS nanocrystals: Effect of indium precursors on their optical properties. *J. Alloy. Compd.* **2016**, *665*, 137–143, doi:10.1016/j.jallcom.2016.01.035.
21. Reiss, P.; Carrière, M.; Lincheneau, C.; Vaure, L.; Tamang, S. Synthesis of semiconductor nanocrystals, focusing on nontoxic and earth-abundant materials. *Chem. Rev.* **2016**, *116*, 10731–10819, doi:10.1021/acs.chemrev.6b00116.
22. Brichkin, S.B.; Razumov, V.F. Colloidal quantum dots: Synthesis, properties and applications. *Russ. Chem. Rev.* **2016**, *85*, 1297, doi:10.1070/rcr4656.
23. Chang, J.; Waclawik, E.R. Colloidal semiconductor nanocrystals: Controlled synthesis and surface chemistry in organic media. *RSC Adv.* **2014**, *4*, 23505–23527, doi:10.1039/C4RA02684E.
24. Gabka, G.; Bujak, P.; Giedyk, K.; Ostrowski, A.; Malinowska, K.; Herbich, J.; Golec, B.; Wielgus, I.; Pron, A. A simple route to alloyed quaternary nanocrystals Ag–In–Zn–S with shape and size control. *Inorg. Chem.* **2014**, *53*, 5002–5012, doi:10.1021/ic500046m.
25. Gabka, G.; Bujak, P.; Kotwica, K.; Ostrowski, A.; Lisowski, W.; Sobczak, J.W.; Pron, A. Luminophores of tunable colors from ternary Ag–In–S and quaternary Ag–In–Zn–S nanocrystals covering the visible to near-infrared spectral range. *Phys. Chem. Chem. Phys.* **2017**, *19*, 1217–1228, doi:10.1039/C6CP07008F.
26. Uematsu, T.; Wajima, K.; Sharma, D.K.; Hirata, S.; Yamamoto, T.; Kameyama, T.; Vacha, M.; Torimoto, T.; Kuwabata, S. Narrow band-edge photoluminescence from AgInS<sub>2</sub> semiconductor nanoparticles by the formation of amorphous III–VI semiconductor shells. *NPG Asia Mater.* **2018**, *10*, 713–726, doi:10.1038/s41427-018-0067-9.
27. Kameyama, T.; Kishi, M.; Miyamae, C.; Sharma, D.K.; Hirata, S.; Yamamoto, T.; Uematsu, T.; Vacha, M.; Kuwabata, S.; Torimoto, T. Wavelength-tunable band-edge photoluminescence of nonstoichiometric Ag–In–S nanoparticles via Ga<sup>3+</sup> doping. *ACS Appl. Mater. Interface.* **2018**, *10*, 42844–42855, doi:10.1021/acsami.8b15222.
28. Shang, H.; Di, Q.; Ji, M.; Bai, B.; Liu, J.; Chen, W.; Xu, M.; Rong, H.; Liu, J.; Zhang, J. From indium-doped Ag<sub>2</sub>S to AgInS<sub>2</sub> nanocrystals: Low-temperature in situ conversion of colloidal Ag<sub>2</sub>S nanoparticles and their nlr fluorescence. *Chem.–Eur. J.* **2018**, *24*, 13676–13680, doi:10.1002/chem.201802973.
29. Doh, H.; Hwang, S.; Kim, S. Size-Tunable Synthesis of nearly monodisperse Ag<sub>2</sub>S nanoparticles and size-dependent fate of the crystal structures upon cation exchange to AgInS<sub>2</sub> nanoparticles. *Chem. Mater.* **2016**, *28*, 8123–8127, doi:10.1021/acs.chemmater.6b04011.
30. Chang, J.-Y.; Wang, G.-Q.; Cheng, C.-Y.; Lin, W.-X.; Hsu, J.-C. Strategies for photoluminescence enhancement of AgInS<sub>2</sub> quantum dots and their application as bioimaging probes. *J. Mater. Chem.* **2012**, *22*, 10609–10618, doi:10.1039/C2JM30679D.
31. Du, Y.; Xu, B.; Fu, T.; Cai, M.; Li, F.; Zhang, Y.; Wang, Q. near-infrared photoluminescent Ag<sub>2</sub>S quantum dots from a single source precursor. *J. Am. Chem. Soc.* **2010**, *132*, 1470–1471, doi:10.1021/ja909490r.

32. Zamiri, R.; Abbastabar Ahangar, H.; Zakaria, A.; Zamiri, G.; Shabani, M.; Singh, B.; Ferreira, J.M.F. The structural and optical constants of Ag<sub>2</sub>S semiconductor nanostructure in the Far-Infrared. *Chem. Cent. J.* **2015**, *9*, 28, doi:10.1186/s13065-015-0099-y.
33. Zhu, G.; Xu, Z. Controllable growth of semiconductor heterostructures mediated by bifunctional Ag<sub>2</sub>S nanocrystals as catalyst or source-host. *J. Am. Chem. Soc.* **2011**, *133*, 148–157, doi:10.1021/ja1090996.
34. Thanh, N.T.K.; Maclean, N.; Mahiddine, S. Mechanisms of nucleation and growth of nanoparticles in solution. *Chem. Rev.* **2014**, *114*, 7610–7630, doi:10.1021/cr400544s.
35. Girma, W.M.; Fahmi, M.Z.; Permadi, A.; Abate, M.A.; Chang, J.-Y. Synthetic strategies and biomedical applications of I–III–VI ternary quantum dots. *J. Mater. Chem. B* **2017**, *5*, 6193–6216, doi:10.1039/C7TB01156C.



© 2019 by the authors. Licensee MDPI, Basel, Switzerland. This article is an open access article distributed under the terms and conditions of the Creative Commons Attribution (CC BY) license (<http://creativecommons.org/licenses/by/4.0/>).